

# Hydrodynamic focusing and interdistance control of particle-laden flow for microflow cytometry

P. K. Shivhare<sup>1,2</sup> · A. Bhadra<sup>1</sup> · P. Sajeesh<sup>1</sup> · A. Prabhakar<sup>2</sup> · A. K. Sen<sup>1</sup> 

Received: 17 January 2016 / Accepted: 14 May 2016 / Published online: 27 May 2016  
© Springer-Verlag Berlin Heidelberg 2016

**Abstract** Single-file focusing and minimum interdistance of micron-size objects in a sample is a prerequisite for accurate flow cytometry measurements. Here, we report analytical models for predicting the focused width of a sample stream  $b$  as a function of channel aspect ratio  $\alpha$ , sheath-to-sample flow rate ratio  $f$  and viscosity ratio  $\lambda$  in both 2D and 3D focusing. We present another analytical model to predict spacing between an adjacent pair of objects in a focused sample stream as a function of sample concentration  $C$ , mobility  $\phi$  of the objects in the prefocused and postfocused regions and flow rate ratio  $f$  in both 2D and 3D flow focusing. Numerical simulations are performed using Ansys Fluent VOF model to predict the width of sample stream in 2D and 3D hydrodynamic focusing for different sample-to-sheath viscosity ratios, aspect ratios and flow rate ratios. Experiments are performed on both planar and three-dimensional devices fabricated in PDMS to demonstrate focusing of sample stream and spacing of polystyrene beads in the unfocused and focused stream at different sample concentrations  $C$ . The predictions of the analytical model and simulations are compared with experimental data, and a good match is found (within 12 %). Further, mobility of objects is experimentally studied in 2D and 3D focusing, and the spread of the mobility data is used as tool for the demonstration of particle focusing in flow cytometer applications.

## 1 Introduction

Microfluidics has important applications in counting and sorting of biological cells (Rodriguez-Trujillo et al. 2007; Jung et al. 2015), microflow cytometry (Golden et al. 2012), cell patterning (Takayama et al. 1999) and biosensors (Justin et al. 2012), which require focusing and separation of objects in microchannels. In microfluidic systems, since the volume of analyte samples is of the order of few microliters, channels of smaller length scales are preferred. Also, investigations of individual biological objects inside microchannels require flow passages of comparable size. However, devices of such smaller channel size are difficult to operate due to clogging (Jung et al. 2015). Thus, most of the microfluidic devices use microchannels of larger than the object size and employ flow focusing for alignment and spacing control of objects before the sorting, analysis or detection modules (Sajeesh et al. 2015).

Dielectrophoresis (Holmes et al. 2006; Yan et al. 2014), acoustophoresis (Chen et al. 2014), magnetophoresis (Zeng et al. 2013) and optophoresis (Kim and Ligler 2010) are some of the active methods used for flow focusing in microfluidics. The main advantage of these methods is that no sheath fluid is required to achieve the flow focusing (Kim and Ligler 2010). However, the use of external fields may affect the biological samples (Jung et al. 2015). Secondly, most of such active techniques provide two-dimensional (2D) focusing only. Additionally, the force applied due to the external field is proportional to particle size, and hence, focusing depends on the particle size (Kim and Ligler 2010). Also, most of the available designs give only 2D focusing. On the other hand, the passive or hydrodynamic focusing techniques are simple and noninvasive techniques that are independent of particle size. Mixing of fluids in a microchannel is very slow (Stone et al. 2004), and thus,

---

✉ A. K. Sen  
ashis@iitm.ac.in

<sup>1</sup> Department of Mechanical Engineering,  
Indian Institute of Technology Madras, Chennai, India

<sup>2</sup> Department of Electrical Engineering,  
Indian Institute of Technology Madras, Chennai, India

two fluids flowing in laminar regime continue to flow side by side without getting mixed (Golden et al. 2012). This property has been extensively used in last two decades to focus or pinch objects present in a sample in a microchannel (Jung et al. 2015). In hydrodynamic focusing, sample fluid is constrained in a channel using a sheath flow and the width of focused sample is generally controlled by the relative flow rates. Flow focusing can be of single phase or multiphase; however, the sample-to-sheath viscosity ratio  $\lambda$  should be limited to 12 % to prevent the Rayleigh–Plateau instability (Selvam et al. 2007).

In 2D hydrodynamic focusing in a typical rectangular microchannel, sample fluid is focused by sheath fluid only in one direction (from two sides out of four sides of the microchannel). 2D focusing is simple to achieve, but it does not focus the sample in the other direction and the sample is not completely isolated from the channel walls, which leads to measurement difficulties. In the case of protein samples, the proteins tend to stick to the wall (Sundararajan et al. 2004), which leads to error in measurement. Similarly, in flow cytometry, 2D focusing does not ensure single-file objects through the optical detection zone as multiple objects can cross the optical window at the same time. Three-dimensional (3D) focusing is required to take care of such difficulties. Conventionally, 3D focusing is achieved by focusing a sample flowing through a nozzle by a sheath fluid through a concentric outer cylindrical channel. Thus, sample is focused surrounded by a sheath from all directions. However, it is difficult to fabricate such a structure using planar fabrication techniques; thus, piecewise approximation of such techniques should be used for 3D focusing (Sundararajan et al. 2004).

The first theoretical model for 2D flow focusing (Stiles et al. 2005) considered an analogous resistance network of the channel to predict the width of the focused stream at various sheath-to-sample flow rate ratios. The model assumes the Hele-Shaw limit of a microchannel (i.e., very high aspect ratio or flow is infinite in the lateral direction). In practical applications, aspect ratio of microchannels may not be very high and the predictions using Hele-Shaw limit are inaccurate. Lee et al. (2006) reported theoretical models for symmetric and asymmetric 2D hydrodynamic flow focusing for any aspect ratio. However, the model assumed the viscosity of the sample and sheath fluid to be the same, which may not be the case in practical applications. A comprehensive analytical model and the validation of the model with experiments in two-dimensional flow focusing have been addressed in the literature (Tripathi et al. 2014). 3D flow focusing has been extensively studied using experiments (Sundararajan et al. 2004; Daniele et al. 2014) and simulations (Chang et al. 2007). However, development of a theoretical model for predicting focused stream width in 3D focusing has not received much attention.

In microfluidics, the two most common detection mechanisms are: (a) electrical detection based on the change in impedance, when the objects pass through a pair of coplanar electrodes (Rodriguez-Trujillo et al. 2007), and (b) optical detection based on the scattering or fluorescence signals, when objects pass through a detection region (Frankowski et al. 2015). The axial interdistance between the objects in a focused sample stream is an important parameter, which could affect the measurements. In electrical or optical detection, if the interdistance between a pair of adjacent objects is smaller than the spacing between the electrodes or width of the optical window, it leads to measurement errors. Both electrical and optical detection techniques require finite response time to differentiate between the different objects that pass through detection region. The response time of the system puts a limit on the maximum flow rate, which can be used in the system. On the other hand, a smaller flow rate leads to a lower throughput of the system. At a fixed flow rate, use of a highly concentrated sample would increase the throughput, but the control of the interdistance between any pair of objects needs to be controlled such that the interdistance is more than the size of the detection window.

In flow cytometry, objects that pass through an optical detection window need to be focused single file and sufficiently spaced out to ensure measurement accuracy. Here, both the focused sample width and the interdistance between the objects in a focused sample stream in 2D and 3D flow focusing are studied theoretically, numerically and further validated with experiments. First, we present theoretical models for 2D and 3D hydrodynamic focusing of sample, which predicts the width of a focused sample stream in a rectangular channel of different aspect ratios  $\alpha$ , sheath-to-sample flow rate ratio  $f$  and viscosity ratios  $\lambda$ . Next, we report another model for the prediction of the spacing between a pair of adjacent objects in 2D and 3D focusing at an optical window. In addition, the VOF model in FLUENT was employed to study the focused sample width in both 2D and 3D flow focusing devices at different operating conditions. We have performed experiments and validated the model in terms of the width of the sample stream in 2D and 3D flow focusing and spacing control between the objects in the focused sample stream. Results of the experiments, analytical model and simulations are compared and discussed.

## 2 Analytical model

### 2.1 2D hydrodynamic focusing

In this section, we derive an analytical model to predict the non-dimensional width of the focused sample stream  $b$  as a function of sheath-to-sample flow rate ratio  $f$ , viscosity

ratio  $\lambda$  and the channel aspect ratio  $\alpha$  for a 2D hydrodynamic focusing device. Consider that sample and sheath fluids are infused at flow rates  $q$  and  $Q$ , respectively, into a straight microchannel of width  $w$  and height  $h$  (aspect ratio  $\alpha = w/h$ ) and length  $L$ . Due to the surrounding sheath fluid, the central sample stream is focused to a narrow stream of width  $a$ , which remains constant downstream, as depicted in Fig. 1a.

We consider uniform, steady, isothermal and incompressible flow of Newtonian fluids (i.e., sample and sheath fluids) and assume the pressure gradient along  $y$  and  $z$  directions to be zero and the body force is negligible. Also, it is assumed that the interface between the sample and sheath fluids is flat at  $y = \frac{a}{2}$ , so that the Young–Laplace pressure drop at the interface vanishes. Under such assumptions, the Navier–Stokes equation which describes the flow of the sample and sheath fluids is reduced to a form given as follows:

$$\mu \left( \frac{\partial^2 u}{\partial y^2} + \frac{\partial^2 u}{\partial z^2} \right) = \frac{\partial p}{\partial x} \tag{1}$$

where  $u$  is velocity of fluid, and  $\mu$  is dynamic viscosity of the fluid. By using the following dimensionless parameters  $\hat{u} = u/u_0$ ,  $\hat{x} = x/L$ ,  $\hat{y} = y/w$ , and  $\hat{z} = z/h$ , and  $P = \frac{h^2}{u_0 \mu L} \frac{\partial p}{\partial x}$ , Eq. 1 can be written in non-dimensional form as follows:

$$\alpha^2 \frac{\partial^2 \hat{u}}{\partial \hat{y}^2} + \frac{\partial^2 \hat{u}}{\partial \hat{z}^2} = \frac{h^2}{u_0 \mu L} \frac{\partial p}{\partial \hat{x}} \tag{2}$$

where  $\alpha$  is the channel aspect ratio. Let  $\mu$  be the viscosity of sample fluid and that  $\eta$  be the viscosity of the sheath fluid. Thus, the Navier–Stokes equations for the sample (region I in Fig. 1a) and sheath fluids (region II in Fig. 1a) can be expressed as follows:

$$\alpha^2 \frac{\partial^2 \hat{u}_1}{\partial \hat{y}^2} + \frac{\partial^2 \hat{u}_1}{\partial \hat{z}^2} = P \tag{3}$$

$$\alpha^2 \frac{\partial^2 \hat{u}_2}{\partial \hat{y}^2} + \frac{\partial^2 \hat{u}_2}{\partial \hat{z}^2} = \frac{P}{\lambda} \tag{4}$$

where  $\hat{u}_1$  and  $\hat{u}_2$  are the flow velocities in the regions I and II, respectively, and  $\lambda = \eta/\mu$  is the sheath-to-sample viscosity ratio. Equation 3 can be solved to obtain the non-dimensional velocity profile in the sample (region I) as

$$\hat{u}_1 = \sum_{n=1}^{\infty} \left[ \frac{-4P}{((2n-1)\pi)^3} + A \times \cosh \left( \frac{(2n-1)\pi}{\alpha} \hat{y} \right) + B \times \sinh \left( \frac{(2n-1)\pi}{\alpha} \hat{y} \right) \right] \sin (2(2n-1)\pi \times \hat{z}) \tag{5}$$

Similarly, Eq. 4 can be solved to obtain the non-dimensional velocity profile in the sheath (region II) as

$$\hat{u}_2 = \sum_{n=1}^{\infty} \left[ \frac{-4P}{((2n-1)\pi)^3} + C \times \cosh \left( \frac{(2n-1)\pi}{\alpha} \hat{y} \right) + D \times \sinh \left( \frac{(2n-1)\pi}{\alpha} \hat{y} \right) \right] \sin (2(2n-1)\pi \times \hat{z}) \tag{6}$$

The constants  $A$ ,  $B$ ,  $C$  and  $D$  in Eqs. 5 and 6 can be obtained by using the following boundary conditions: (a) no-slip boundary condition at the wall and the interface, (b) velocity profile is symmetric, and thus, gradient is zero, i.e.,  $\frac{\partial \hat{u}_1}{\partial \hat{y}} = 0$  at the center of the channel, i.e., at  $\hat{y} = 0$ , (c) shear stress is continuous, i.e.,  $\mu \frac{\partial \hat{u}_1}{\partial \hat{y}} = \eta \frac{\partial \hat{u}_2}{\partial \hat{y}}$ , and velocity is continuous, i.e.,  $\hat{u}_1 \left( \frac{b}{2}, z \right) = \hat{u}_2 \left( \frac{b}{2}, z \right)$  at the flat interface between the two fluids, i.e., at  $\hat{y} = \frac{b}{2}$ , where  $b$  is the

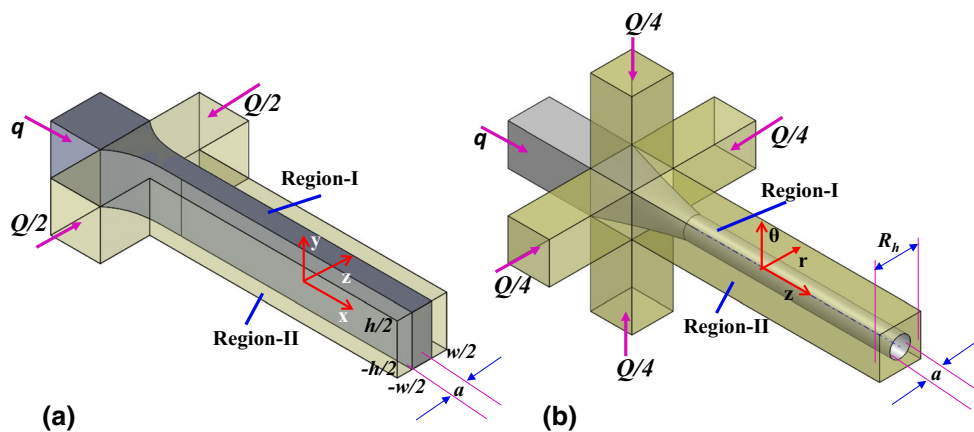


Fig. 1 Schematic diagram of a 2D flow focusing device, b 3D flow focusing device

non-dimensional width of the focused sample stream (i.e.,  $a$  non-dimensionalized with width of the channel  $w$ ), and (d) velocity of fluid is zero, i.e.,  $\hat{u}_2(y = 1/2, z) = 0$  at wall fluid interface, i.e., at  $\hat{y} = 1/2$ . Use of these boundary conditions in Eqs. 5 and 6 provides following Eqs. 7–10, which are solved to obtain the unknowns  $A, B, C$  and  $D$ .

$$B = 0, \tag{7}$$

$$\beta A \times \sinh\left(\frac{(2n-1)\pi b}{2\alpha}\right) = C \times \sinh\left(\frac{(2n-1)\pi b}{2\alpha}\right) + D \times \cosh\left(\frac{(2n-1)\pi b}{2\alpha}\right), \tag{8}$$

$$A \times \cosh\left(\frac{(2n-1)\pi b}{2\alpha}\right) = C \times \cosh\left(\frac{(2n-1)\pi b}{2\alpha}\right) + D \times \sinh\left(\frac{(2n-1)\pi b}{2\alpha}\right), \tag{9}$$

and

$$\frac{-4P}{((2n-1)\pi)^3} = C \times \cosh\left(\frac{(2n-1)\pi}{2\alpha}\right) + D \times \sinh\left(\frac{(2n-1)\pi}{2\alpha}\right). \tag{10}$$

Now, the sample and sheath flow rates can be determined by integrating the velocity profile across the flow cross sections in the respective regions as  $Q = \iint u(y, z) dy dz$ . Upon integration, the flow rates of the sample (in region I) and sheath (in region II) are expressed as

$$q = 4 \times \sum_{n=1}^{\infty} \left[ \frac{-2Pb}{((2n-1)\pi)^4} + \frac{A\alpha}{((2n-1)\pi)^2} \times \sinh\left(\frac{(2n-1)\pi b}{2\alpha}\right) \right] \tag{11}$$

$$Q = 4 \times \sum_{n=1}^{\infty} \left[ \frac{-2P(1-b)}{((2n-1)\pi)^4} + \frac{\alpha}{((2n-1)\pi)^2} (C \times X + D \times Y) \right] \tag{12}$$

where

$$X = \left[ \sinh\left(\frac{(2n-1)\pi}{2\alpha}\right) - \sinh\left(\frac{(2n-1)\pi b}{2\alpha}\right) \right] \tag{13}$$

$$Y = \left[ \cosh\left(\frac{(2n-1)\pi}{2\alpha}\right) - \cosh\left(\frac{(2n-1)\pi b}{2\alpha}\right) \right] \tag{14}$$

Finally, sheath-to-sample flow rate ratio  $f$  can be expressed as  $f = Q/q$ . As observed, sheath-to sample flow rate ratio  $f$  is a function of aspect ratio  $\alpha$ , focused sample width  $b$  and viscosity ratio  $\lambda$ . For a fixed flow rate ratio  $f$ , aspect ratio  $\alpha$  and viscosity ratio  $\lambda$ , Eqs. 11–14 are solved using MATLAB to evaluate the non-dimensional width  $b$  of the focused sample stream or vice versa.

## 2.2 3D hydrodynamic focusing

Here, we derive an analytical model to predict the non-dimensional width of the focused sample stream  $b$  as a function of sheath-to-sample flow rate ratio  $f$ , viscosity ratio  $\lambda$  and the channel aspect ratio  $\alpha$  in a 3D hydrodynamic focusing device. A schematic of the 3D flow focusing arrangement is shown in Fig. 1b. The sheath fluids are infused into the channel in both horizontal and vertical directions for focusing of the sample stream. Let the sample and sheath fluids are infused at a flow rate of  $q$  and  $Q$ , respectively, into the microchannel device. Various works (Kim et al. 2009; Sen and Bhardwaj 2012; Nawaz et al. 2014; Testa et al. 2015; and Zhuang et al. 2008) based on different focusing principles reported that, when a sample is focused using 3D hydrodynamic focusing, the cross section of the focused sample stream at steady-state condition is nearly elliptical or circular depending on the aspect ratio of the channel and the sheath-to-sample flow rate ratio. At an aspect ratio of 1 ( $\alpha = \frac{w}{h}$ ), and flow rate ratio of  $f = 1$ , the cross section of the focused sample stream was found to be circular. It is observed from our 3D numerical simulations reported in the manuscript at Sect. 5.2 that the cross section of the focussed stream is nearly circular in shape. However, as the aspect ratio of the channel increases or the flow rate ratio increases, the cross section of the focused stream is less circular and more elliptical in shape, similar to that reported in the literature (Kim et al. 2009). The analytical model for 3D hydrodynamic focusing was derived by considering the focused sample stream to be cylindrical in shape. Development of a model by considering a focused stream as elliptical in cross section inside a rectangular channel is extremely challenging, and a closed form expression could not be reached. So we proceeded with cylindrical coordinates system. Let  $a$  be the hydraulic radius of focused stream, while  $R_h$  be the hydraulic radius of the microchannel. Assuming the fluid to be Newtonian, uniform, steady, isothermal and incompressible and considering the pressure gradient along  $\theta$  and  $z$  directions to be zero and negligible body force, the velocity profile in cylindrical coordinates is expressed as follows:

$$U = -\frac{\Delta p}{\mu L} \frac{r^2}{4} + c_1 \ln(r) + c_2 \tag{15}$$

The above equation is written for the sample (region I) and sheath (region II) as

$$U_1 = -\frac{\Delta p}{\mu L} \frac{r^2}{4} + c_1 \ln(r) + c_2 \tag{16}$$

$$U_2 = -\frac{\Delta p}{\eta L} \frac{r^2}{4} + c_3 \ln(r) + c_4 \tag{17}$$

where  $\mu$  and  $\eta$  are the viscosities of the sample (region I) and sheath (region II) fluids, respectively, where  $r$  is the distance from the center of channel and  $c_1, c_2, c_3$  and  $c_4$  are constants, which are determined using the following boundary conditions: (a) no-slip boundary condition at the wall and the interface (b) velocity is symmetric, and thus, gradient is zero, i.e.,  $\frac{\partial u_1}{\partial r} = 0$ , at the center of the channel, i.e., at  $r = 0$ , (c) shear stress is continuous, i.e.,  $\mu \frac{\partial u_1}{\partial r} = \eta \frac{\partial u_2}{\partial r}$ , and velocity is continuous, i.e.,  $u_1(a) = u_2(a)$  at interface between the two fluids, i.e., at  $r = a$ , (d) velocity of fluid is zero, i.e.,  $u_2(R_h) = 0$  at wall fluid interface, i.e., at  $r = R_h$ . Using these boundary conditions in Eqs. 16 and 17, the velocity profiles are obtained as follows:

$$U_1 = \frac{\Delta p}{4L} \left( \frac{a^2 - r^2}{\mu} + \frac{R_h^2 - a^2}{\eta} \right) \tag{18}$$

$$U_2 = \frac{\Delta p}{4\eta L} (R_h^2 - r^2) \tag{19}$$

Now, the sample and sheath flow rates are determined by integrating the velocity profile across the flow cross sections in the respective regions as  $Q = \iint u(r) r dr d\theta$ . Upon integration, the flow rates of the sample (in region I) and sheath (in region II) are expressed as

$$q = \frac{\pi \Delta p}{4L} \left( \frac{a^4}{2\mu} + \frac{a^2(R_h^2 - a^2)}{\eta} \right) \tag{20}$$

$$Q = \frac{\pi \Delta p}{8\eta L} (R_h^4 - a^2(2R_h^2 - a^2)) \tag{21}$$

Finally, the sheath-to-sample flow rate ratio  $f$  can be expressed as  $f = \frac{Q}{q}$ , if we substitute for  $Q$  and  $q$  from Eqs. 20 and 21, respectively, and rearranging the terms, we get

$$b^4(f \times \lambda - 2f - 1) + 2b^2(f + 1) - 1 = 0 \tag{22}$$

where  $\lambda$  is the viscosity ratio of the sheath-to-sample fluid,  $b$  is the normalized width of the focused sample stream, i.e., the ratio of hydraulic radius of the focused stream  $a$  to the hydraulic radius of the channel  $R_h$ . As observed, the sheath-to sample flow rate ratio  $f$  is a function of aspect ratio  $\alpha$ , non-dimensional focused sample width  $b$  and viscosity ratio  $\lambda$ . For a fixed flow rate ratio  $f$ , aspect ratio  $\alpha$  and viscosity ratio  $\lambda$ , Eq. 22 is solved to evaluate the non-dimensional width of focused stream  $b$ .

### 2.3 Interdistance of focused objects

Next, we present a theoretical model to predict the spacing between the objects in a sample fluid before the flow focusing region (i.e., region 1) and in the flow focusing region

prior to the optical window (i.e., region 2). A schematic of the relative position of two objects in regions 1 and 2 is depicted in Fig. 2. The interdistance  $g_1$  between a pair of adjacent objects in the region 1 depends on the sample concentration  $C$ . The width of the optical window  $l_{opt}$  depends on the size of the focused beam crossing the microchannel in flow cytometry. In case of samples containing objects at high concentrations (e.g., blood sample or concentrated cell sample), the interdistance between a pair of adjacent objects passing through the optical window  $g_2$  should be greater than the width of the optical window  $l_{opt}$  to enable detection of individual objects and avoid error due to multiple objects crossing the optical window simultaneously. Here, we present a theoretical model which predicts the interdistance between a pair of adjacent objects in the focused region, for a sample of a given concentration and flow rate ratio. Recently, we reported a theoretical model (Sajeesh et al. 2015), which can be used for the prediction of interdistance between a pair objects present in a sample focused using a secondary fluid as:

$$\frac{g_2}{g_1} = 1 + \frac{\phi_{f2}}{\phi_{b1}}(1 + f) - \frac{\phi_{f1}}{\phi_{b1}} \tag{23}$$

where  $\phi$  is the mobility of object, which is defined as the ratio of velocity of object to the superficial velocity of fluid inside the microchannel. The subscripts  $f$  and  $b$  refer to the front and back object in a pair of adjacent objects, and similarly, subscripts 1 and 2 refer to the regions 1 and 2, respectively. In our earlier work (Sajeesh et al. 2015), it was assumed that the size of the objects is comparable to that of the channel size so the mobility of the objects in region 1 was found to be a function of object size only. However, in practical flow cytometry applications, the size of the objects is much smaller than the channel size to avoid clogging. Thus, the mobility of the objects considered here is a function of the object size as well as its position with respect to the channel centerline  $d^*$ . The variation of the mobility of objects with its position from the channel centerline  $d$  (non-dimensionalized with respect to

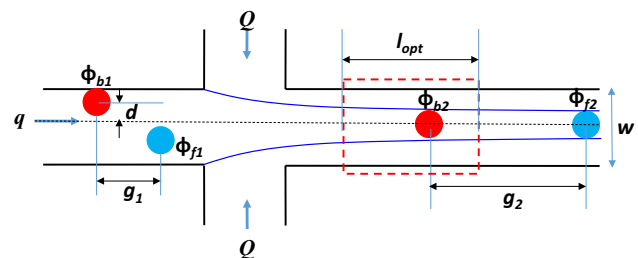


**Fig. 2** Schematic of the separation distance between a pair of objects in the unfocused region  $g_1$  and focused region  $g_2$  of a 2D or 3D hydrodynamic focusing device; optical window is indicated using dotted lines



channel width  $w$ ) is discussed in Sect. 5.3. The variation of the interdistance between a pair of adjacent objects in region 1, i.e.,  $g_1$  with the concentration of the objects  $C$  in a sample, is discussed in Sect. 5.3. In the limiting case, the interdistance between the objects in the focused region  $g_2$  must be equal to length of optical window  $l_{opt}$ ; thus, the minimum flow rate ratio  $f_{min}$  at which device is to be operated is obtained as:

$$f_{min} = \left( \frac{l_{opt}}{g_1} + \frac{\phi_{f1}}{\phi_{b1}} - 1 \right) \frac{\phi_{b1}}{\phi_{f2}} - 1 \quad (24)$$

Thus, for a given sample concentration  $C$  or  $g_1$  and mobilities, the minimum flow rate ratio  $f_{min}$  required to avoid passing of multiple objects through the optical window simultaneously can be calculated. As concentration  $C$  increases, the throughput of the system increases, but  $g_1$  decreases, and thus,  $g_2$  decreases, which may lead to measurement errors if  $g_2 < l_{opt}$ . Similarly, if flow rate ratio  $f$  increases, separation distance between the objects  $g_2$  increases, but since superficial velocity of fluid also increases, the residence time of object in the optical window decreases. If the residence time of the object in the optical window is less than time constant of the optical system, it leads to measurement error. Thus, depending on the sample concentration  $C$ , the flow rate ratio  $f$  should be selected to provide simultaneous focusing and separation control to achieve high throughput and accurate measurements. The above model can be used to predict the spacing between the objects both in 2D and 3D hydrodynamic focusing of samples in a microchannel.

### 3 Numerical model

Numerical simulations are carried out using ANSYS Fluent Volume of Fluid (VOF) model to predict the width of the focused sample stream  $b$  in case of both 2D and 3D hydrodynamic focusing. The symmetric and axisymmetric nature of the model geometry, respectively, in case of 2D and 3D is used to reduce the computational efforts. The velocity boundary conditions are used at the inlets, and atmospheric pressure boundary condition is applied at the outlet. Grid independence studies are performed, and the required minimum number of grids in 2D hydrodynamic simulations in a channel of aspect ratio  $\alpha = 1$  was found to be 6,78,542 and for the 3D hydrodynamic simulations in a channel of aspect ratio  $\alpha = 1$  was found to be 8,70,673. The pressure and momentum discretization scheme, pressure velocity coupling and interface reconstruction scheme used in the simulations are detailed elsewhere (Sajeesh et al. 2014). A fixed surface tension of 0.035 mN/m was taken into account between the sample and sheath. Numerical simulations are

obtained at various flow rate ratios  $f$  (1.0–6.0), aspect ratios  $\alpha$  (0.4–1.4) and viscosity ratios  $\lambda$  (1.55–41.68) in both 2D and 3D flow focusing.

## 4 Experiments

### 4.1 Device fabrication

The microchannel devices used for the 2D and 3D flow focusing were fabricated using standard photolithography followed by soft lithography process. Photolithography was used to prepare a silicon master with a patterned layer of photoresist SU8 2075 (MicroChem Corp, Newton, USA). Then, soft lithography was used to mold the 2D and 3D flow focusing devices using polydimethylsiloxane (PDMS) as the substrate material. A detailed description of the photolithography and soft lithography procedure is provided elsewhere (Sajeesh et al. 2014). Schematic of the 2D and 3D flow focusing devices is depicted in Fig. 3a, b, respectively. The 2D flow focusing device comprises two layers: a PDMS layer that contains channels for the horizontal focusing, which is bonded with a glass layer as shown in Fig. 3c. The 3D flow focusing device comprises two PDMS layers: a top layer that contains a channel for horizontal focusing of the sample and an inlet hole for infusing the sheath fluid to vertically focus the sample from the top. The bottom layer contains one inlet for the sheath fluid to further focus the sample from the bottom so that sample will be focused from all the four directions.

### 4.2 Materials and methods

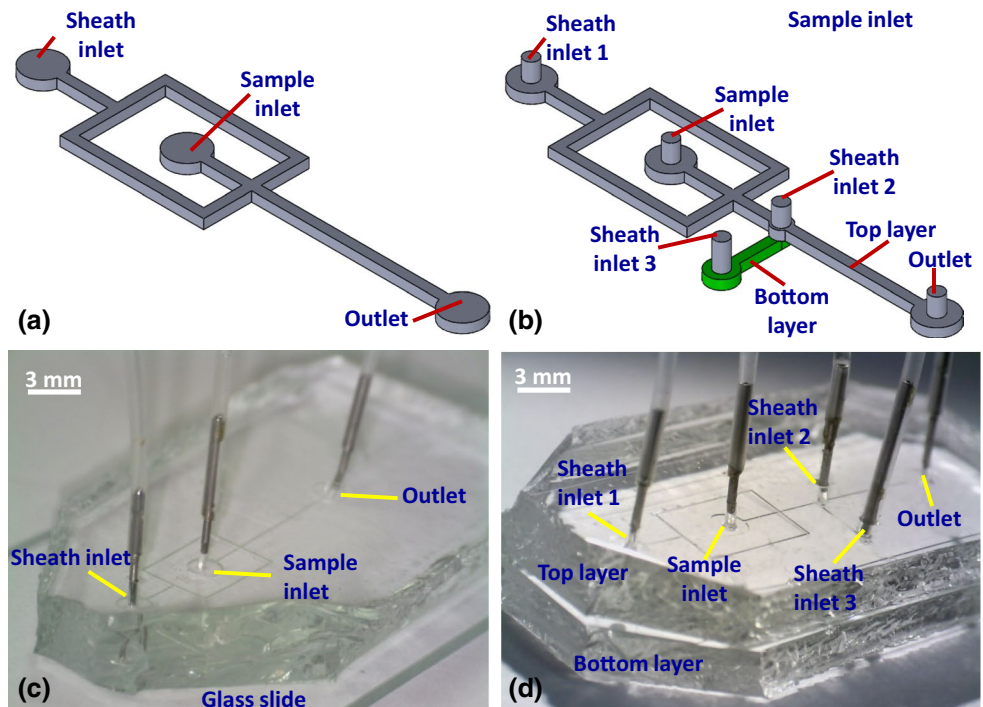
#### 4.2.1 DI water and aqueous glycerol

DI water mixed with dye was taken as the sample fluid, and aqueous glycerol (Sigma-Aldrich, Bangalore, India) solution with 20, 40, 60 and 80 % wt/wt was used as the sheath fluid. The corresponding viscosity ratio (of the sheath to sample) is 1.55, 3.21, 8.52 and 41.68, respectively. Both the sample and sheath solutions were filtered using nylon 0.2- $\mu$ m filters (Axiva Sicheem Biotech, Chennai, India) to avoid channel clogging. The properties of the sample and sheath fluids used in our experiments are reported in our earlier work (Sajeesh et al. 2014).

#### 4.2.2 Microbeads

Polystyrene beads (Sigma-Aldrich, Bangalore, India) of 10  $\mu$ m diameter were suspended in aqueous glycerol of 22 % wt/wt to avoid sedimentation. 0.5 % wt/wt of surfactant Tween 80 (Sigma-Aldrich, Bangalore, India) was added to the solution to prevent the aggregation of the

**Fig. 3** **a** Schematic of the 2D flow focusing device. **b** Schematic of the 3D flow focusing device. **c** Image of a 2D flow focusing device. **d** Image of the 3D flow focusing device



beads present in the solution. The number of beads  $N_p$  in 1.0  $\mu\text{L}$  of original bead sample (from vendor) was calculated as follows:

$$N_p = \frac{6 \times 10^{10} (W_v \%) }{\pi \rho_p D^3} \quad (25)$$

where  $W_v \%$  is latex concentration in original bead sample,  $\rho_p$  is the density of polystyrene, and  $D$  is the diameter of the beads. Using the available data, the number of beads  $N_p$  was calculated to be 90,510 beads/ $\mu\text{L}$ . The original bead solution was diluted with the aqueous solution so that the concentrations  $C$  of beads in the sample fluid were 0.4739, 0.9478, 2.3695, 3.7912 and 4.739  $\mu\text{L}/\text{mL}$ .

### 4.3 Experimental setup

Syringe pumps were used for infusing the sample and sheath fluids into the microchannel. An inverted microscope (Axiovert A1, Carl Zeiss GmbH, Germany) coupled with high-speed camera (SA3, Photron, USA) and florescent attachment (HBO illuminator, Carl Zeiss GmbH, Germany) was used. The high-speed camera interfaced with the computer through a software (Photron Fastcam Viewer, Photron, USA) was used to observe and capture the hydrodynamic focusing. In 3D flow focusing, an additional syringe pump with a T-connector was used to infuse the sheath fluid for focusing in the vertical direction. The focused sample width  $b$  was captured using high-speed camera (1000 fps) at a fixed resolution ( $1024 \times 1024$  pixels) and

magnification ( $\times 10$ ). The captured images of the focused sample stream were analyzed using Image J software (Rasband, W. S., ImageJ, USA). First of all, grayscale profiles of the images were created along a straight line across the channel, and the interface location was precisely identified by setting a threshold intensity value which is average of the maximum (sheath) and minimum intensities (sample). Further, the focused sample width  $b$  was measured using the options provided in the software by scaling the non-dimensional widths of the sample stream and channel with that of the actual dimension of the channel. In our experiments with beads, images were captured at 4000 fps in order to track the beads accurately.

## 5 Results and discussion

### 5.1 2D flow focusing

Volume fraction contours of the sample in 2D flow focusing obtained from the numerical simulations are depicted in Fig. 4. The simulation and experimental images of 2D flow focusing for various flow rate ratios  $f$  are also depicted in Fig. 4. We have measured the width of the focused sample stream at least 10 times at each experimental condition, and the standard deviation of the data is reported as the error bar. The width of the sample stream  $a$  in numerical simulations is measured by considering the volume fraction  $\psi = 0.5$  at the sample sheath interface. Non-dimensional focused stream width obtained from model and numerical

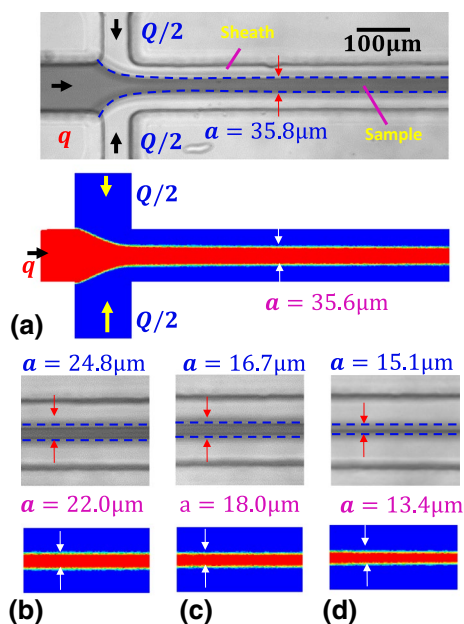
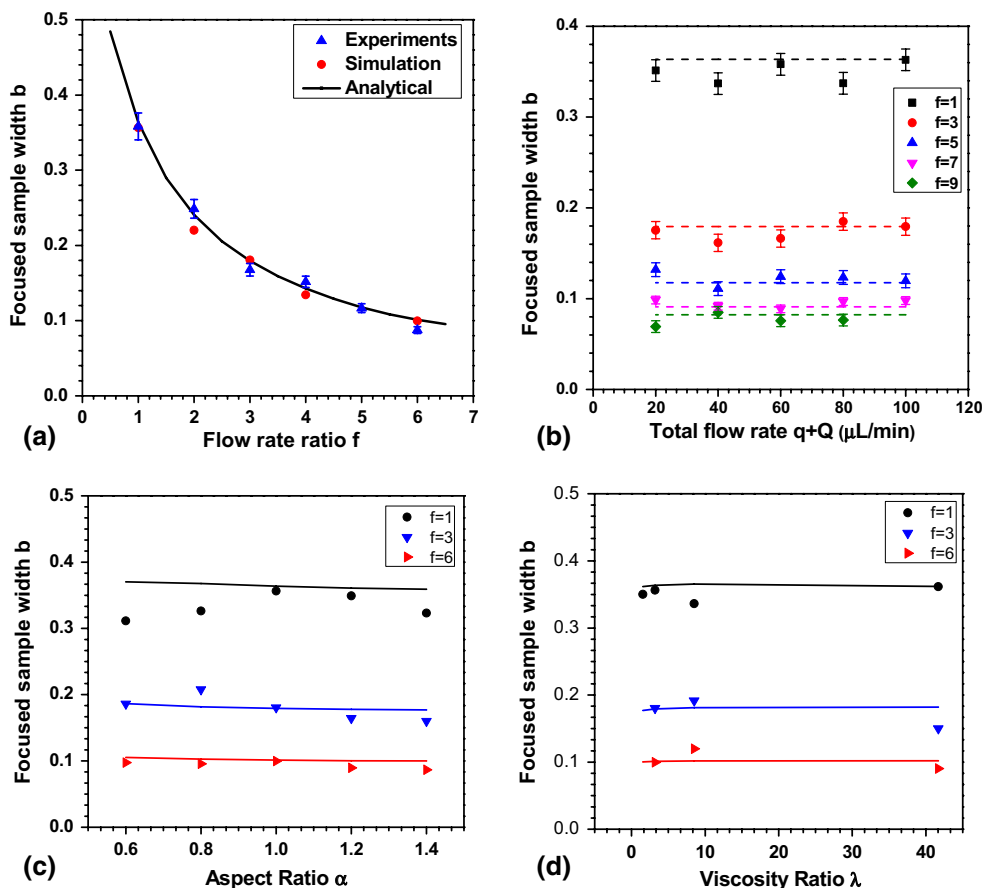


**Fig. 4** Simulation and experimental results for 2D flow focusing a  $f = 1.0$ , b  $f = 2.0$ , c  $f = 3.0$  and d  $f = 4.0$ , DI water as sample fluid and 20 % glycerol as sheath fluid in a microchannel of aspect ratio  $\alpha = 1$

simulations is compared with that obtained from experiments, as shown in Fig. 5a. The non-dimensional focused width can be controlled by varying flow rate ratio  $f$ ; however, flow rate ratio  $f$  can be varied between a maximum and minimum value to avoid cutoff of sample and sheath fluids, respectively (Knight et al. 1998). The theoretical and numerical values are found to be in good agreement with experimental data with maximum error of 12 %, as shown in Fig. 5a. The flow rate ratio  $f$  was varied from 1.0 to 6.0, and as a result, the corresponding non-dimensional stream width  $b$  was found to vary from 0.3636 to 0.1012, respectively. The Reynolds number for the flow varied between 2.48 and 8.93, respectively. In our experiments, the sample flow rate was kept constant, while the sheath flow rate was varied to obtain the various flow rate ratios  $f$ . The effect of total flow rate (i.e., sheath + sample flow rates) entering the microfluidic chip on width of focused flow was studied, as shown in Fig. 5b. From Fig. 5a, b, it is observed that focused width  $b$  reduces as the flow rate ratio  $f$  increases, but this change is significant at lower values of  $f$ . The rate of change of  $b$  decreases at higher values of  $f$ , and hence, the width of the focused stream  $b$  does not change much at higher values of  $f$ . This is also evident from Fig. 5b, where

**Fig. 5** a 2D flow focusing: variation of non-dimensional focused stream width  $b$  with flow rate ratio  $f$ : comparison of model, simulations and experiments at aspect ratio  $\alpha = 1$  and viscosity ratio  $\lambda = 3.21$ . b Variation of  $b$  with the total flow rate  $q + Q$  and various flow rate ratios  $f$ , at an aspect ratio  $\alpha = 1$  and viscosity ratio  $\lambda = 3.21$ : comparison of model (solid lines) and experiments (symbols with error bars). c Variation of  $b$  with aspect ratio  $\alpha$  at a flow rate ratio  $f = 1$  and viscosity ratio  $\lambda = 3.21$ . d Variation of  $b$  with viscosity ratios at a flow rate ratio  $f = 1$  and aspect ratio  $\alpha = 1$ : comparison of model (solid lines) and numerical simulations (symbols)





focused width  $b$  changes significantly at lower flow rate ratios  $f$ .

Numerical simulations are performed to study the effect of the aspect ratio  $\alpha$  of the microchannel at a fixed flow rate ratio  $f = 1$ . Non-dimensional focused stream width  $b$  obtained from the numerical simulations at different channel aspect ratios  $\alpha$  is compared with that obtained using analytical model in Fig. 5c. It is observed that width of the focused sample is independent of the aspect ratio  $\alpha$  of the microchannel in 2D flow focusing. The theoretical values are found to be in good agreement with the numerical data within 15 %. Further, numerical simulations are performed to study the effect of sheath-to-sample viscosity ratio on the focused stream width at  $f = 1$  in a microchannel of aspect ratio  $\alpha = 1$ . From Fig. 5d, it is observed that width of the sample stream is independent of the sheath-to-sample viscosity ratio.

### 5.2 3D flow focusing

Numerical simulations were performed to demonstrate 3D flow focusing. The isometric view of the volume fraction contours obtained from the numerical simulations is presented in Fig. 6a. As observed, the interface between the sample and sheath is smooth and does not have sharp corners to avoid infinite shear stress. From Fig. 6a, b, it is observed that at an aspect ratio  $\alpha = 1$ , for a flow rate ratio of  $f = 1$ , the cross section of core sample is nearly circular in shape. The flow rate ratio  $f$  can be adjusted to achieve the required sample stream width  $b$ . Sample stream width obtained from the numerical simulations and the experiments at different flow rate ratios is shown in Fig. 6b–d. With DI water as the sample fluid and 40 % glycerol as the sheath fluid, the lateral

size of the focused sample stream predicted using the model presented in Sect. 2.2 and obtained from the numerical simulations is compared with the experimental data for 3D flow focusing, as shown in Fig. 7a. The results of the analytical model derived assuming cylindrical sample core are also compared with the experimental results. It is observed that, at a low flow rate ratio  $f = 1$ , in a rectangular channel of aspect ratio  $\alpha = 1$ , width of the sample stream  $b$  obtained from theoretical model and experimental results matches within an error of  $<1\%$ . So the assumption of focused cylindrical sample core inside the rectangular channel, used in the 3D flow focusing derivation, is valid. For aspect ratio  $\alpha = 1$ , as the flow rate ratio increases to  $f = 3$ , error between the model and experimental result increases to 10 %. However, as the flow rate ratio increases further above  $f = 4$ , error progresses to 25 %. This error is attributed to the assumption of focused cylindrical core sample used in the analytical model. Further, numerical simulations are performed to study the effect of viscosity ratio  $\lambda$  and aspect ratio  $\alpha$  on the non-dimensional focused sample width  $b$ , and the results are compared with that obtained using the analytical model. It is observed that aspect ratio  $\alpha$  of the channel has negligible effect on the focused sample width as shown in Fig. 9b. From Fig. 9c, it can be seen that non-dimensional width  $b$  reduces with the increase in sheath-to-sample viscosity ratio  $\lambda$ , and this change is significant at lower values of viscosity ratios  $\lambda$ . For instance, at a flow rate ratio  $f = 1$ , non-dimensional focused width  $b$  reduces from 0.55 to 0.45 when viscosity ratio  $\lambda$  increases from 1.54 to 8.52, but it reduces from 0.45 to 0.34 as  $\lambda$  increases from 8.52 to 41.68. The numerical solution matches with theoretical solution with maximum error of 8 %.

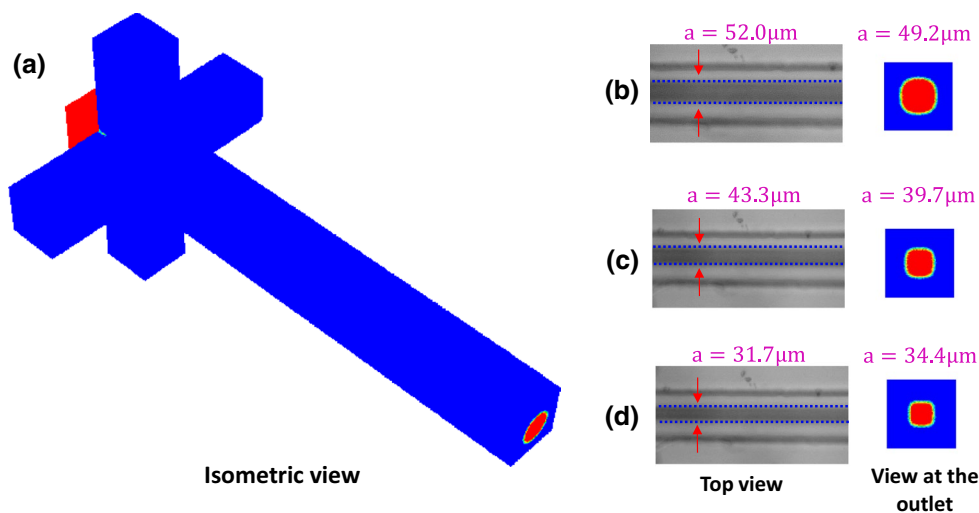


**Fig. 6** a Isometric view of phase fraction contour of a 3D flow focusing device obtained from numerical simulations, b comparison of focused stream width obtained from numerical simulations and

experiments at flow rate ratios  $f = 1.0$ , c  $f = 2.0$ , d  $f = 3.0$  in a microchannel of aspect ratio  $\alpha = 1$  and viscosity ratio  $\lambda = 3.21$

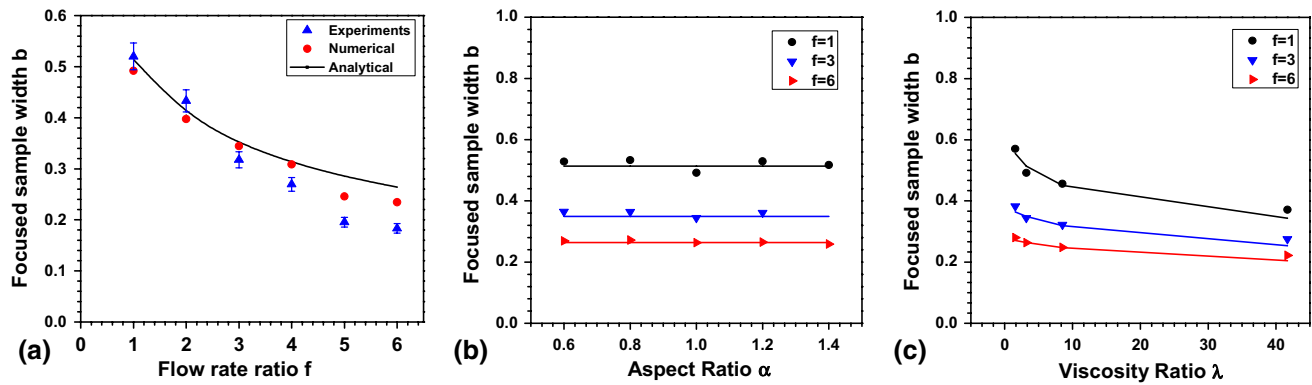


**Fig. 7** **a** 3D flow focusing device: variation of non-dimensional focused width  $b$  with flow rate ratio  $f$ : comparison of model, simulations and experiments at aspect ratio  $\alpha = 1$  and viscosity ratio  $\lambda = 3.21$ . **b** Variation of  $b$  with aspect ratio  $\alpha$  at a flow rate ratio  $f = 1$

and viscosity ratio  $\lambda = 3.21$ : comparison of model and simulations. **c** Variation of  $b$  with viscosity ratios at a flow rate ratio  $f = 1$  and aspect ratio  $\alpha = 1$ : comparison of model and simulations

### 5.3 Characterization of separation distance

The separation distance of objects in the focused region  $g_2$  is a function of separation distance in unfocused region  $g_1$ , mobility of beads in unfocused and focused regions and flow rate ratio  $f$ . Mobility  $\phi$  and normalized distance from the wall  $d^* = \frac{d}{w}$  of a large number of beads were measured experimentally in unfocused and focused regions for different flow rate ratios  $f$  at a constant sample flow rate  $q$ . For large number of microbeads, mobility in unfocused region  $\phi$  was plotted against normalized distance from the wall  $d^*$ . Mobility of beads  $\phi$  in the unfocused region can be correlated with the normalized distance from the wall  $d^*$  as follows:

$$\phi = A + Bd^* + Cd^{*2} \quad (26)$$

where the values of  $A$ ,  $B$  and  $C$  were found to be 1.68, 0.22, and  $-1.95$ , respectively. The correlation was found by curve fitting of a large set of experimental data in MATLAB with  $R^2$  value of 0.93 and 95 % confidence bound. From Fig. 8, it can be observed that the mobility profile is parabolic along the width of the channel, as expected. Similarly, the mobility of large number of beads was also measured in the focused region. Since the beads are focused at the center of the channel, the mobility does not vary much and was found to be almost constant. The mobility in focused region is calculated to be 1.2 with standard deviation of 0.082.

The probable distance between the objects  $g_1$  before reaching the focusing region for different concentrations of particle-laden flow  $C$  is studied experimentally. Different concentrations of polystyrene beads  $C$  were prepared as explained in the experimental section. At each concentration  $C$ , large number of beads in unfocused region was considered and the distance between the beads just before

entering the focused region was measured. The data for each concentration were fitted to a Gaussian curve with the  $R^2$  value of from 0.71 to 0.96, as shown in Fig. 8b. For each concentration  $C$ , the mean value from the Gaussian fit was considered to calculate the initial separation distance  $g_1$ . Finally, in Fig. 8c, various values of separation distance  $g_1$  are plotted against sample concentration  $C$ , as follows:

$$g_1 = g_o + A \exp\left(-\frac{C}{t}\right) \quad (27)$$

where the values of  $g_o$ ,  $A$  and  $t$  were found to be 15.45, 52.71 and 1.41, respectively. This correlation was found by curve fitting of a large set of experimental data in MATLAB with  $R^2$  value of 0.99 and 95 % confidence bound. Figure 8b shows that the separation distance  $g_1$  decreases with the increase in the sample concentration  $C$ . Using Eq. 27 along with Eq. 23, separation distance between the beads in the focused region can be theoretically predicted for any given sample concentration  $C$ , which is plotted in Fig. 8d. Since the theoretical model for the spacing of the objects includes flow rate ratio of the sheath to sample  $f$ , mobility of the object  $\phi$  in the unfocused and focused sample regions, this model can be used for both 2D and 3D hydrodynamic focusing. The comparison between the model predictions and experimental data shows good match within 15 % as shown in Fig. 8d. For the same flow rate ratio  $f$  and uniform size of the particles in the sample, mobility of the objects remains fixed at different concentrations, and thus,  $g_2$  is directly correlated with  $g_1$ . However, the separation distance in unfocused region  $g_1$  depends on the concentration  $C$  of the sample. At low concentration range, as the concentration  $C$  increases, the separation distance between the particles  $g_1$  in the unfocused region decreases significantly. But at higher concentrations above 4  $\mu\text{L}/\text{mL}$  (concentration of solid particles in sample),

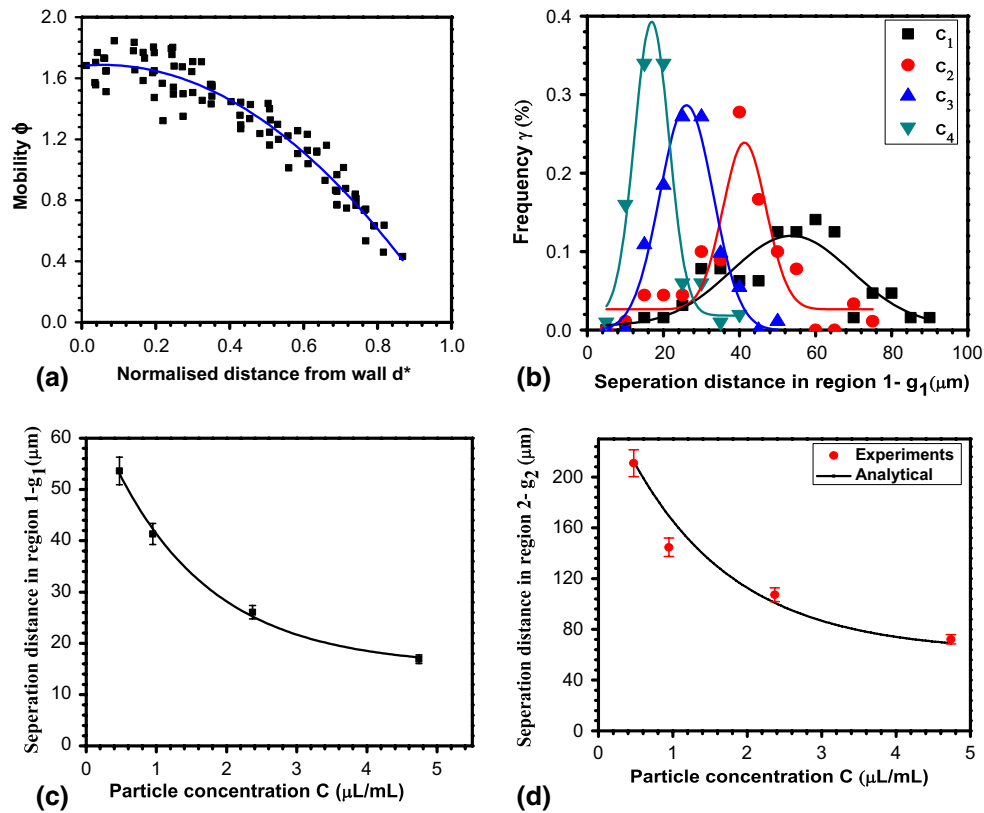


**Fig. 8** **a** The variation of mobility  $\phi$  of objects in the unfocused region with non-dimensional distance  $d^*$  from the channel centerline. **b** The variation of separation distance  $g_1$  between beads with sample

concentration  $C$ . **c** Comparison of model with experimental result for the variation of separation distance  $g_2$  with sample concentration  $C$ , at a flow rate ratio of  $f = 1.0$

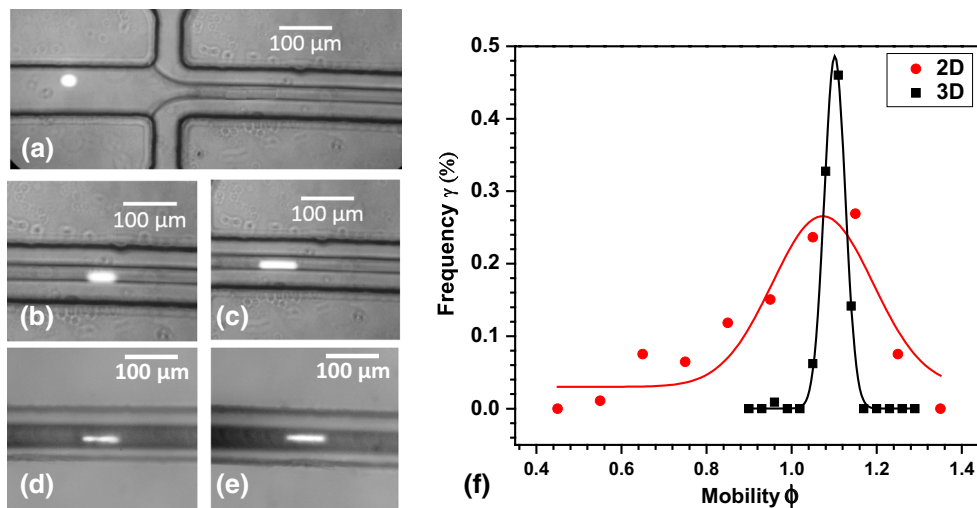


**Fig. 9** **a** Microbeads in the sample at the unfocused region. **b, c** Variation in streak length of beads in 2D flow focusing. **d, e** Equal streak length of beads in 3D flow focusing. **f** Normalized number of counts with mobility of microbeads in 2D and 3D flow focusing

the variation in spacing between the objects in the unfocused region is negligible, as shown in Fig. 8c. This could be because of the shear-induced diffusion forces which

prevent particles from getting closer any further at higher concentrations. Similar observations can be found in the literature (Torquato 1995).

#### 5.4 Mobility of objects in 2D and 3D flow focusing

Experiments were performed with fluorescence microbeads to focus them at the center of the channel, as shown in Fig. 9. In 2D flow focusing, since the sample stream is not focused in the vertical directions, beads in the focused stream can move at different positions across the channel height. So the mobility (Sajeesh et al. 2014) of the beads which are moving closer to the center of the channel are higher as compared to that are moving closer to the wall. Thus, depending on the position of the beads across the channel height, their mobility will be different as observed from the different streak lengths ( $94 \pm 33 \mu\text{m}$ ) in Fig. 9b, c. The varying mobility of beads and multiple beads passing through a detection region would introduce measurement error in flow cytometry as explained in Sect. 2.3 of the paper. Thus, 3D flow focusing is necessary to avoid such measurement error. In 3D flow focusing, the samples are focused from all the directions and beads in the samples will be focused close to the centerline of the channel. So mobility of the beads passing through the focused stream will be fixed which is observed from the equal streak length ( $107 \pm 9 \mu\text{m}$ ) of fluorescence beads in a 3D flow focused device as shown in Fig. 9d, e.

The fluorescence microbeads (of size  $15 \mu\text{m}$ ) were passed and efficiently focused at the center of the channel. Using a large set of experimental data, the mobility of beads is plotted against its normalized number of counts  $\gamma$  in case of both 2D and 3D flow focusing devices, as presented in Fig. 9f. In 2D focusing, particles are focused single file only in the horizontal (width) direction, but in the vertical (height) direction, the particles are still unfocused. The unfocused particles in 2D focusing also get influenced by the inertial lift forces and tend to align some distance away from the centerline (typically 0.6–0.8 times channel dimension), which is indicated by mobility  $\sim 1.1$  (note—mobility is maximum  $\sim 1.3$  at the center). So the frequency–mobility curve need not be symmetric (as the particle focusing is not exactly half-way between the center and the top/bottom walls). However, in 3D focusing, since the particles are focused both horizontally and vertically, these focused particles have only chance to get distributed over the lateral dimension (width) of the focused stream due to which the frequency–mobility curve is symmetric, as shown in Fig. 9f. The data are fitted to a Gaussian function to evaluate the variation of mobility across channel height. The  $R^2$  value for 2D Gaussian fit was 0.76, while for 3D Gaussian fit, it was 0.99. The width of the Gaussian curve was found to be 0.23 and 0.049 for 2D and 3D flow focusing, respectively.

Since the  $Re$  of the flow in the focused stream is  $>1$ , there are two inertial lift forces viz. wall-induced lift force  $F_w$  (objects tend to migrate from wall toward the center)

and shear-induced lift force  $F_s$  (objects tend to migrate from the center toward the channel wall) that act on the objects (Amini et al. 2014). The objects attain an equilibrium position across the section of the channel depending upon the balance between the lift forces, and the net lift force  $F_L$  acting on an object is given as  $F_L = C_L G^2 \rho k^4$ , where  $C_L$  is the non-dimensional lift coefficient,  $G$  is the shear rate,  $\rho$  is the density of the sample, and  $k$  is the radius of the objects in the sample. The cross-stream migration distance  $L_m$  of the object due to the inertial flow focusing is given as (Zhou and Papautsky 2013),

$$L_m = \frac{2\rho L u_1 C_L k^3}{3\pi \mu D_h^2} \quad (28)$$

where  $L$  is the length of the channel,  $u_1$  is the velocity of the sample, and  $D_h$  is the hydraulic diameter of the channel. For our channel dimensions and fluid properties, objects could only migrate  $4 \mu\text{m}$  from the centerline of the channel even at the maximum flow rate  $Re \sim 9$ . However, the length of the channel required for achieving the equilibrium position is estimated to be  $>5 \text{ cm}$  (Di Carlo 2009; Amini et al. 2014), which is much longer than the length of the channel used in the present device (i.e., 2 cm). So in the present scenario, the inertial migration has small effect on the lateral migration of the objects, which will be mostly focused within the sample stream.

## 6 Conclusion

In this work, we reported analytical models for predicting the non-dimensional width of sample stream  $b$  in both 2D and 3D flow focusing in terms of flow rate ratio  $f$ , aspect ratio  $\alpha$  and viscosity ratio  $\lambda$ . In both 2D and 3D flow focusing, the width of the sample stream is found to decrease with the increase in the flow rate ratio. The width of the sample stream is independent of the aspect ratio of the channel and sheath-to-sample viscosity ratio at a fixed flow rate ratio. In 2D flow focusing, the focused stream width predicted using the analytical model and obtained from simulations was compared with that obtained from experiments, which showed good match within 12 %. The focused stream width was found to be independent of the individual flow rates of the sample or sheath stream and is solely a function of the flow rate ratio. 3D flow focusing was demonstrated using model, simulations and experiments. In 3D flow focusing, width of the sample stream  $b$  obtained from theoretical model and experimental results matches within an error of  $<1 \%$ . As the flow rate ratio increases further above  $f = 4$ , error in the focused stream width predicted from model and the experiments

progresses to 25 % which is attributed to the assumption of focused cylindrical core sample used in the analytical model. Further another theoretical model was derived to predict the interdistance between the particles in a sample in the unfocused region as a function of concentration and the distance between them in the focused sample at different flow rate ratios in 2D and 3D flow focusing. The interdistance in the focused region with sample concentration predicted using the model was compared with that obtained from experiments, and the match was found to be within 15 %. The comparison between these model predictions and experimental data shows good match within 15 %. In 2D flow focusing, since the sample stream is not focused in the vertical direction, the mobility of the focused beads was found to vary depending on their position across the channel height, which clearly indicated the need for 3D focusing. The variation of the mobilities of beads across the channel height was evaluated by plotting the frequency of occurrence with bead mobility. It was found that the spread of the bead mobility is significantly smaller in 3D focusing, indicating that the beads are focused close to the channel centerline. The proposed method along with a dedicated confocal microscopy setup could give a complete picture of 3D hydrodynamic focusing of objects at an optical window.

**Acknowledgments** The authors would like to thank DST and DBT India and IIT Madras for providing the financial support for the project. We thank Chemical Engineering Department IIT Madras, for providing an additional syringe pump which was required for the experiments. We acknowledge MEMS Lab, Department of EE, IIT Madras, for supporting with the photolithography work. The authors also acknowledge P. G. Senapathy Computer Center, IIT Madras, for providing Virgo cluster facility for the simulations. Our special thanks to Interdisciplinary Program, IIT Madras, which enabled this work.

## References

- Amini H, Lee W, Di Carlo D (2014) Inertial microfluidic physics. *Lab Chip* 14:2739–2761. doi:10.1039/c4lc00128a
- Chang CC, Huang ZX, Yang RJ (2007) Three-dimensional hydrodynamic focusing in two-layer polydimethylsiloxane (PDMS) microchannels. *J Micromech Microeng* 17(8):1479–1486
- Chen Y, Nawaz AA, Zhao Y et al (2014) Standing surface acoustic wave (SSAW)-based microfluidic cytometer. *Lab Chip* 14:916–923. doi:10.1039/c3lc51139a
- Daniele MA, Boyd DA, Mott DR, Ligler FS (2014) 3D hydrodynamic focusing microfluidics for emerging sensing technologies. *Biosens Bioelectron* 67:25–34. doi:10.1016/j.bios.2014.07.002
- Di Carlo D (2009) Inertial microfluidics. *Lab Chip* 9:3038–3046. doi:10.1039/b912547g
- Frankowski M, Simon P, Bock N et al (2015) Simultaneous optical and impedance analysis of single cells: a comparison of two microfluidic sensors with sheath flow focusing. *Eng Life Sci* 15:286–296. doi:10.1002/elsc.201400078
- Golden JP, Justin GA, Nasir M, Ligler FS (2012) Hydrodynamic focusing—a versatile tool. *Anal Bioanal Chem* 402:325–335. doi:10.1007/s00216-011-5415-3
- Holmes D, Morgan H, Green NG (2006) High throughput particle analysis: combining dielectrophoretic particle focussing with confocal optical detection. *Biosens Bioelectron* 21:1621–1630. doi:10.1016/j.bios.2005.10.017
- Jung H, Chun M-S, Chang M-S (2015) Sorting of human mesenchymal stem cells by applying optimally designed microfluidic chip filtration. *Analyst* 140:1265–1274. doi:10.1039/c4an01430h
- Justin GA, Denisin AK, Nasir M et al (2012) Hydrodynamic focusing for impedance-based detection of specifically bound microparticles and cells: implications of fluid dynamics on tunable sensitivity. *Sensors Actuators, B Chem* 166–167:386–393. doi:10.1016/j.snb.2012.02.077
- Kim JS, Ligler FS (2010) *The Microflow Cytometer*. PAN Stanford Publishing, Singapore. ISBN 9789814267410
- Kim DS, Kim DS, Han K, Yang W (2009) An efficient 3-dimensional hydrodynamic focusing microfluidic device by means of locally increased aspect ratio. *Microelectron Eng* 86:1343–1346. doi:10.1016/j.mee.2009.01.017
- Knight J, Vishwanath A, Brody J, Austin R (1998) Hydrodynamic focusing on a silicon chip: mixing nanoliters in microseconds. *Phys Rev Lett* 80:3863–3866. doi:10.1103/PhysRevLett.80.3863
- Lee G-B, Chang C-C, Huang S-B, Yang R-J (2006) The hydrodynamic focusing effect inside rectangular microchannels. *J Micromechanics Microengineering* 16:1024–1032. doi:10.1088/0960-1317/16/5/020
- Nawaz AA, Zhang X, Mao X et al (2014) Sub-micrometer-precision, three-dimensional (3D) hydrodynamic focusing via “microfluidic drifting”. *Lab Chip* 14:415–423. doi:10.1039/c3lc50810b
- Rodriguez-Trujillo R, Mills CA, Samitier J, Gomila G (2007) Low cost micro-Coulter counter with hydrodynamic focusing. *Microfluid Nanofluidics* 3:171–176. doi:10.1007/s10404-006-0113-8
- Sajeesh P, Doble M, Sen AK (2014) Hydrodynamic resistance and mobility of deformable objects in microfluidic channels. *Biomicrofluidics* 8:1–23. doi:10.1063/1.4897332
- Sajeesh P, Manasi S, Doble M, Sen AK (2015) Microfluidic device with focusing and spacing control for resistance based sorting of droplets and cells. *Lab Chip* 15:3738–3748. doi:10.1039/C5LC00598A
- Selvam B, Merk S, Govindarajan R, Meiburg E (2007) Stability of miscible core—annular flows with viscosity stratification. *J Fluid Mech* 592:23–49. doi:10.1017/S0022112007008269
- Sen AK, Bhardwaj P (2012) Microfluidic system for rapid enumeration and detection of microparticles. *J Fluids Eng* 134:111401. doi:10.1115/1.4007805
- Stiles T, Fallon R, Vestad T et al (2005) Hydrodynamic focusing for vacuum-pumped microfluidics. *Microfluid Nanofluidics* 1:280–283. doi:10.1007/s10404-005-0033-z
- Stone HA, Stroock AD, Ajdari A (2004) Engineering flows in small devices. *Annu Rev Fluid Mech* 36:381–411. doi:10.1146/annurev.fluid.36.050802.122124
- Sundararajan N, Pio MS, Lee LP, Berlin AA (2004) Three-dimensional hydrodynamic focusing in polydimethylsiloxane (PDMS) microchannels. *J Microelectromechanical Syst* 13:559–567. doi:10.1109/JMEMS.2004.832196
- Takayama S, McDonald JC, Ostuni E, et al (1999) Patterning cells and their environments using multiple laminar fluid flows in capillary networks. In: *Proceedings of the National Academy of Sciences of the United States of America*. pp 5545–5548
- Testa G, Persichetti G, Bernini R (2015) Micro flow cytometer with self-aligned 3D hydrodynamic focusing. *Biomed Opt Express* 6:54–62. doi:10.1364/BOE.6.000054
- Torquato S (1995) Nearest-neighbour statistics for packings of hard spheres and disks. *Phys Rev E* 51:3170–3182. doi:10.1103/PhysRevE.51.3170
- Tripathi S, Chakravarty P, Agrawal A (2014) On non-monotonic variation of hydrodynamically focused width in a rectangular microchannel. *Curr Sci* 107:1260–1274



- Yan S, Zhang J, Li M et al (2014) On-chip high-throughput manipulation of particles in a dielectrophoresis-active hydrophoretic focuser. *Sci Rep* 4:5060. doi:[10.1038/srep05060](https://doi.org/10.1038/srep05060)
- Zeng J, Deng Y, Vedantam P et al (2013) Magnetic separation of particles and cells in ferrofluid flow through a straight microchannel using two offset magnets. *J Magn Magn Mater* 346:118–123. doi:[10.1016/j.jmmm.2013.07.021](https://doi.org/10.1016/j.jmmm.2013.07.021)
- Zhou J, Papautsky I (2013) Fundamentals of inertial focusing in microchannels. *Lab Chip* 13:1121–1132. doi:[10.1039/c2lc41248a](https://doi.org/10.1039/c2lc41248a)
- Zhuang GS, Jensen TG, Kutter JP (2008) Three-dimensional hydrodynamic focusing over a wide reynolds number range using a two-layer microfluidic design. Twelfth international conference on miniaturized systems for chemistry and life sciences 2008. San Diego, California, pp 1357–1359